To show that the emitted photons originate from within the cavity, we tuned the cavity off-resonance by changing the thickness of the active layer and found no resonant emission. When the output reflector is replaced by a 5.5-period PPV DBR, we obtain a higher cavity finesse ($\Delta\lambda$ = 16 nm), but at the expense of efficiency. Moreover, the large optical dispersion of the PPV DBR should also be useful to reduce the off-axis color shift (*26*).

Our approach allows the refractive index of polymer semiconductors to be varied without altering the energies of their electron- and hole-transport states, so that charge transport across the layer interfaces remains facile. This contrasts with the situation when different semiconductors are used, for example, in GaAs/AlGaAs DBRs (*27*).

We conclude that separate manipulation and thus orthogonal design of the optical, electronic, and transport properties of semiconducting polymers are feasible. This may enable the fabrication of a new generation of organic semiconductor optoelectronic devices with refractive index and carrier transport level profiles that are functional.

References and Notes

1. A. Dodabalapur *et al.*, *Appl. Phys. Lett.* **73**, 142 (1998).
2. H. Sirringhaus, N. Tessler, R. H. Friend, *Science* **280**, 1741 (1998).
3. A. J. Heeger, *Solid State Commun.* **107**, 673 (1998).
4. R. H. Friend *et al.*, *Nature* **397**, 121 (1999).
5. S. Brittain, K. Paul, X.-M. Zhao, G. Whitesides, *Phys. World* 1998, 31 (May 1998).
6. D. W. V. Krevelen, *Properties of Polymers: Their Correlation with Chemical Structure, Their Numerical Estimation and Prediction from Additive Group Contributions* (Elsevier, Amsterdam, ed. 3, 1990).
7. M. P. Pileni, *J. Phys. Chem.* **97**, 6961 (1993).
8. S. A. Carter, J. C. Scott, P. J. Brock, *Appl. Phys. Lett.* **71**, 1145 (1997).
9. B. J. Schwartz, F. Hide, M. A. Díaz-García, M. R. Andersson, A. J. Heeger, *Philos. Trans. R. Soc. London Ser. A* **355**, 775 (1997).
10. A. Yamamori, C. Adachi, T. Koyama, Y. Taniguchi, *Appl. Phys. Lett.* **72**, 2147 (1998).
11. C. C. Han and R. L. Elsenbaumer, *Synth. Met.* **30**, 123 (1989).
12. N. Tessler, N. T. Harrison, R. H. Friend, *Adv. Mater.* **10**, 64 (1998).
13. H. Yokoyama, *Science* **256**, 66 (1992).
14. E. F. Schubert *et al.*, *ibid.* **265**, 943 (1994).
15. D. G. Lidzey *et al.*, *Nature* **395**, 53 (1998).
16. T. Granlund *et al.*, *Chem. Phys. Lett.* **288**, 879 (1998).
17. T. Nakayama, Y. Itoh, A. Kakuta, *Appl. Phys. Lett.* **63**, 594 (1993).
18. R. H. Jordan, L. J. Rothberg, A. Dodabalapur, R. E. Slusher, *ibid.* **69**, 1997 (1996).
19. J. Grüner, F. Cacialli, R. H. Friend, *J. Appl. Phys.* **80**, 207 (1996).
20. P. W. M. Blom, H. F. M. Schoo, M. Matters, *Appl. Phys. Lett.* **73**, 3914 (1998).
21. J. C. Carter *et al.*, *ibid.* **71**, 34 (1997).
22. A. Sakamoto, Y. Furukawa, M. Tasumi, *J. Phys. Chem. B* **101**, 1726 (1997).
23. A. C. Arias, M. G. Granström, D. S. Thomas, R. H. Friend, *Phys. Rev. B*, in press.
24. M. G. Harrison, K. E. Ziemelis, R. H. Friend, P. L. Burn, A. B. Holmes, *Synth. Met.* **55**, 218 (1993).
25. E. F. Schubert, N. E. J. Hunt, R. J. Malik, M. Micovic, D. L. Miller, *J. Lightwave Technol.* **14**, 1721 (1996).
26. N. Tessler, S. Burns, H. Becker, R. H. Friend, *Appl. Phys. Lett.* **70**, 556 (1997).
27. K. Tai, L. Yang, Y. H. Wang, J. D. Wynn, A. Y. Cho, *ibid.* **56**, 2496 (1990).
28. This work has been partially supported by the European Commission under Brite-Euram contract BRPR-CT97-0469 ("OSCA") and by the Engineering and Physical Sciences Research Council. We thank Cambridge Display Technology (Cambridge, UK) for materials, R. A. L. Jones and A. Wehrum for the spectroscopic ellipsometer facility, and E. P. Woo at The Dow Chemical Company (Midland, MI) for support. P.K.H.H. is on study leave from the National University of Singapore and thanks St. John's College (Cambridge, UK) and the Institute of Materials Research and Engineering (Singapore) for funding.

25 March 1999; accepted 8 June 1999

Role of Fluids in Faulting Inferred from Stress Field Signatures

Jeanne L. Hardebeck* and Egill Hauksson

The stress orientation signature of weak faults containing high-pressure fluids has been observed for segments of the San Andreas fault system in southern California. The inferred lithostatic fluid pressures extend into the surrounding relatively intact rock in a zone scaling with the width of the interseismic strain accumulation. Repeated strain-related fracturing and crack sealing may have created low-permeability barriers that seal fluids into the network of currently active fractures.

It is crucial for understanding fault evolution and the dynamics of large earthquakes to determine why numerous major faults, including the San Andreas in California, are weak (*1–3*). Fault zone fluids at high (~lithostatic) pressures could lower the effective normal stress on a fault, decreasing its shear strength (*2*). Alternatively, weak faults may contain inherently weak materials, although laboratory testing has eliminated most candidate minerals (*4*). A third model is dynamic weakening, in which fault strength reduces during slip (*5*).

Each model contains predictions about the orientation of the maximum principal stress axis σ_1. For a strong fault, σ_1 should be at ~30° to the fault plane (*3*). If the fault is dynamically weak, σ_1 is predicted to be at a higher angle, which is controlled by the frictional resistance during slip. Some rotation toward lower angles near the fault may occur because of interseismic loading of the fault. However, if typical interseismic stress changes of ~5 MPa (*6*) are to rotate the stress field ≥10°, the background deviatoric stress must be ≤15 MPa (*7*). Crustal stress is typically near the laboratory-predicted frictional strength of rock (*8*), which, over seismogenic depths, corresponds to an average deviatoric stress of ~50 MPa (*9*). Rotations of ≥10° therefore imply weak material.

A stress state is predicted to develop inside a fault zone of weak materials (either inherently weak or weakened by high-pressure fluids) that is distinct from that outside (*10, 11*). An increase in fault-parallel stress inside the fault zone, which suppresses hydrofracture in the case of high fluid pressure, rotates the principal stress axes (Fig. 1). The model predicts σ_1 to be at high angles to the fault (≥60°) outside the fault zone and at lower angles (≤60°) inside (Fig. 1C).

We use stress orientations determined from earthquake focal mechanisms to look for evidence of stress rotation across the San Andreas fault system in southern California, which consists of three major right-lateral strike-slip faults: the San Andreas (SAF), San Jacinto (SJF), and Elsinore (EF). We have compiled a catalog of about 50,000 earthquakes recorded by the California seismic networks (Fig. 2). The earthquakes along eight profiles across relatively straight segments of the SAF, SJF, and EF are inverted for the direction of maximum horizontal stress σ_H (Figs. 2 and 3). We interpret our observations in terms of the models presented above. For fault segments that parallel the relative plate motion (Fig. 3, profiles A, F, G, and H), far-field σ_H is typically ~60° to the fault trend. However, within 2 to 5 km of the Parkfield and Indio segments of the SAF (Fig. 3, A and G), the northern and southern SJF (Fig. 3, F and H), and the central and southern EF (Fig. 3, G and H), σ_H is at ~40° to the fault trend.

In the region of the compressional bend in the SAF (profiles B, C, D, and E) far-field σ_H is typically ~90° to the fault trend. Near the Fort Tejon (Fig. 3B) and San Bernadino (Fig. 3D) segments of the SAF, however, σ_H is at ~40° to the fault trend. The zone of stress rotation across the Fort Tejon segment is 20 to 30 km wide, whereas that across the San Ber-

Seismological Laboratory, MC 252-21, California Institute of Technology, Pasadena, CA 91125, USA.

*To whom correspondence should be addressed. E-mail: jlh@gps.caltech.edu

nadino segment is ~5 km wide and superimposed on a wider zone (30 to 50 km) to the northeast where σ_H is ~50° to the fault (*12*). Previous studies of stress orientation along the SAF have also found a principal stress axis oblique to the Fort Tejon and San Bernadino segments (*13*). The Mojave segment of the SAF (Fig. 3C) has a broad zone (50 to 90 km) in which σ_H is at ~60° to the fault. Banning (Fig. 3E) is the only segment of the SAF where σ_H is everywhere >60° to the fault. The Banning segment is unlike the rest of the SAF in having numerous strands, some nonvertical, and may not contain a single through-going fault (*14*), so a difference in stress state is not surprising.

In general, σ_H makes an angle of 40° to 50° to the fault trend inside a zone along the fault about 2 to 50 km wide, and about 60° to 90° further away (Figs. 2 and 3). Profiles produced with different binning schemes, data subsets, or a different inversion method (*15*) agree to within the 95% confidence intervals. The σ_H orientations near the faults are robust and are not artifacts of poor data quality or inadequate focal mechanism diversity (Fig. 4). Stress orientations for different depth intervals are also similar, which suggests that all stresses scale with the lithostatic load.

The observed rotation of σ_H from about 60° to 90° in the far field to ~40° along the fault indicates a zone of low shear strength because of either high fluid pressures or inherently weak materials. We prefer the high fluid pressure interpretation, as a suitable weak mineral has yet to be identified (*4*). The orientation of far-field σ_H relative to the faults implies ~lithostatic fluid pressures in the fault zones (*16*). The inferred average frictional force over seismogenic depths varies from ~0, for segments where far-field σ_H is ~90° to the fault, to ~50 MPa, for segments where it is ~60° to the fault.

High pore pressures can be maintained by low-permeability barriers. Mineral deposition could decrease permeability, sealing fluids inside the fault zone. Extensive mineralization has been observed in exhumed fault zones (*17*), and fluid sealing has been observed in the laboratory (*18*). In one explanation, fluids are constantly fed from the lower crust into the relatively permeable fault zone and are maintained there at high pressures (*10*). Alternatively, the fault zone permeability decreases and pore pressure increases between earthquakes, and coseismic fracturing increases permeability and releases fluids (*19*). Both scenarios are consistent with ~lithostatic pore pressure in the fault zone.

The wide (>5 km) zones of rotated σ_H imply that high-pressure fluids are also present in the relatively intact rock surrounding the faults. The narrower (2 to 5 km) zones are at the limit of the resolution (the width of the data bins), but the wider zones (>5 km) are well resolved. Low-permeability barriers are again the most likely mechanism for maintaining high fluid pressures. Core samples from the Cajon Pass drill hole, ~5 km from the SAF, exhibit unusually low permeabilities, primarily due to crack sealing (*20*).

The width of the inferred zone of high fluid pressure scales roughly with the width of the interseismic strain accumulation across the faults. In the western Transverse Ranges (the Fort Tejon and Mojave segments of the SAF) where the zone of apparent high fluid pressure is widest (20 to 90 km), a wide zone of strain accumulation (>40 km) is observed geodetically (*21*). To the southeast (the San Ber-

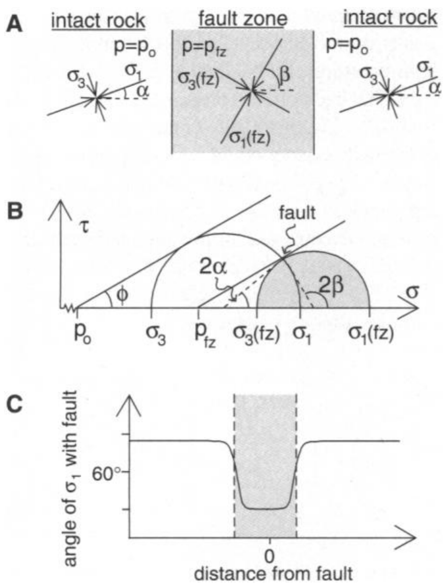

Fig. 1. Stress field signature of a weak fault zone containing high-pressure fluids, modified from (*10*). (**A**) A two-dimensional view perpendicular to the fault. The pore pressure in the surrounding intact rock is hydrostatic, p_o. The maximum and minimum principal stress axes, σ_1 and σ_3, are in the plane of the cross section, and σ_1 makes a small angle, α, with the normal to the fault. The fault zone pore pressure, p_{fz}, is elevated and the stress orientations differ from that of the intact rock, σ_1(fz) making angle $\beta > \alpha$ with the normal to the fault plane. (**B**) Mohr circle representation of the same stress states. Open semicircle represents the stress state in the intact rock, and shaded semicircle represents the fault zone. The point common to the two circles is the fault orientation. The Coulomb failure envelopes for pore pressures of p_o and p_{fz} are shown, and ϕ is the angle of internal friction. (**C**) Sketch of the expected orientation of σ_1 relative to the fault trend versus perpendicular distance from the fault. Shading indicates zone of high fluid pressure.

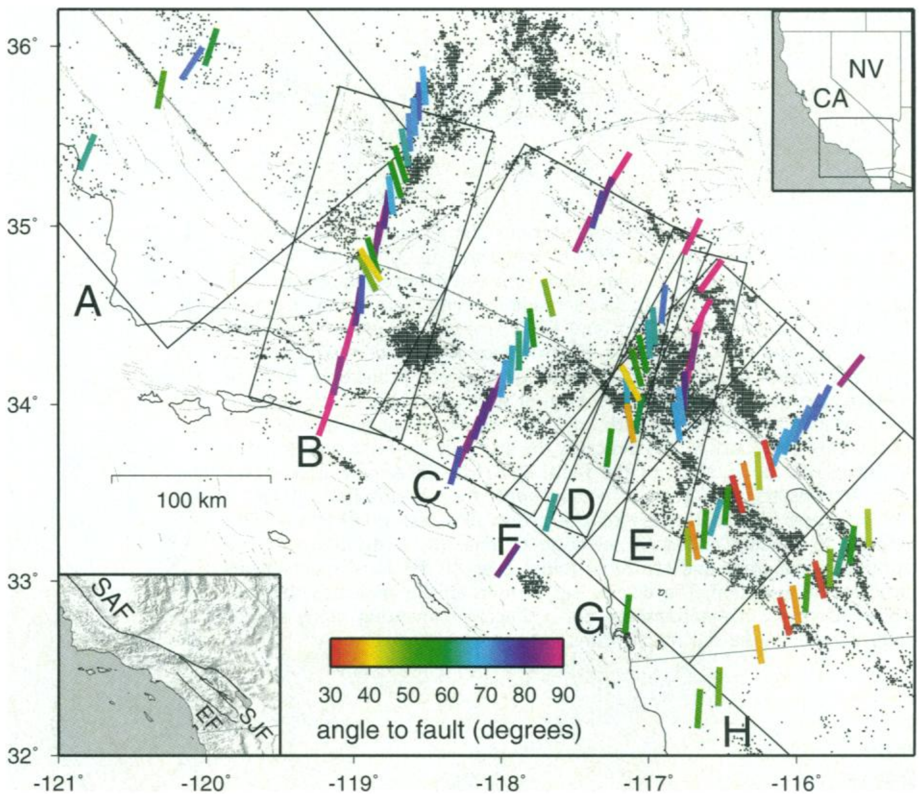

Fig. 2. Map view of ~50,000 southern California earthquakes, 1981–1998. The earthquakes were relocated and first-motion focal mechanisms were found with a three-dimensional velocity model (*27*). All events have location uncertainties of ≤1 km and ≥12 first-motion picks. Stress orientations are found along profiles A to H. Bar orientation indicates direction of σ_H, the maximum horizontal stress, and the color denotes the angle σ_H makes with the strike of the nearest major fault segment. The σ_H axis is typically at a low angle to the fault in the near field and approximately perpendicular in the far field, consistent with the high-pressure fluid model (Fig. 1). Boxes indicate events used for the profiles. (Insets) Location of SAF, SJF, and EF.

nadino and Indio segments of the SAF, and the SJF and EF), where the zone of apparent high fluid pressure is narrower (<20 km), the strain accumulation is also more localized (<20 km) (*21*). The wider zones of strain accumulation across the segments that failed in the 1857 Fort Tejon earthquake (*22*) are apparently at odds with postseismic relaxation models that predict broadening of strain accumulation with time since the last earthquake (*23*).

These observations suggest the following model. Strain accumulation is not entirely elastic and may cause extensive fracturing. Low permeability materials trap fluids into the network of currently active fractures, and, if fluid-filled cracks are pervasive, high pore pressures would be accompanied by a stress rotation. As fractures become inactive, they seal, further contributing to low permeability. Fractures and fluids modify the elastic properties of the rock, reinforcing strain localization unrelated to the time since the last earthquake.

Zones of low resistivity and low seismic velocity, some as wide as 10 to 20 km, have been observed across faults in California, New Zealand, and Japan (*24*), presumably due to high-pressure fluids. Elevated fluid pressures have also been observed during drilling near the SAF (*25*). High-pressure fluids in the San Andreas fault system could have important implications for earthquake rupture mechanics. During rupture, shear heating increases pore pressure and encourages further slip, and fault dilation decreases pore pressure and discourages slip. These competing mechanisms may result in complex rupture behavior (*26*).

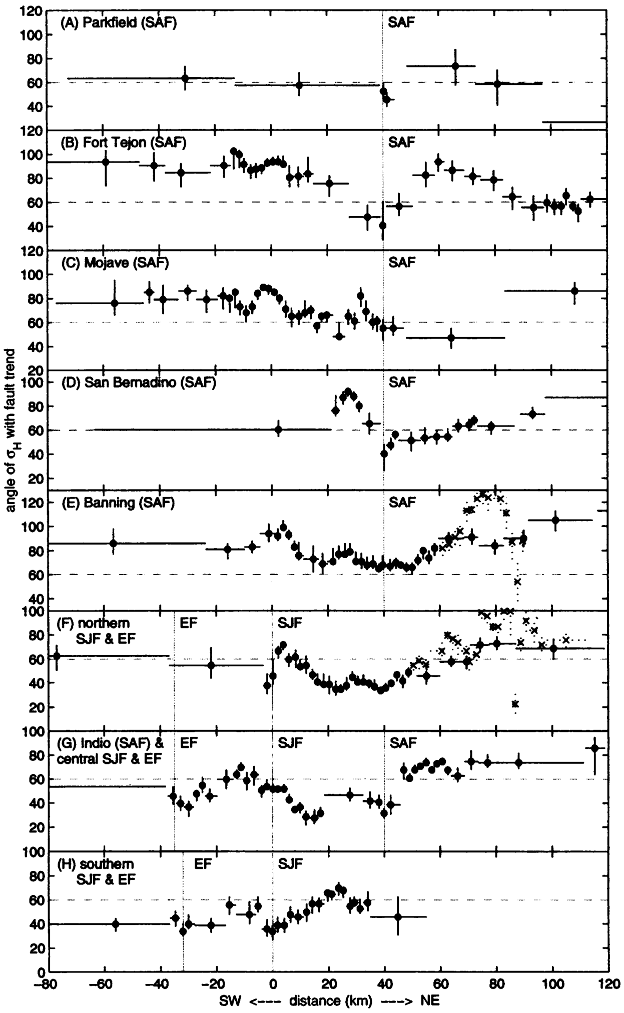

Fig. 3. Direction of σ_H relative to the trend of the fault segment versus perpendicular distance. Earthquakes along each profile (Fig. 2) are binned in groups of 100 based on their perpendicular distance from the fault (along the fault trace, a 2-km-wide bin is used), and each group is inverted for principal stress orientation by a standard method (*28*). Horizontal error bars indicate the width of the bins, and vertical error bars indicate the 95% confidence interval of the inversion results. Vertical gray lines indicate approximate location of the fault segment traces (only parallel segments are included in a single profile). Horizontal dashed line at 60° is for reference, and angles of 90° indicate left-lateral stress orientations. Crosses with dotted error bars are post-1992 Landers earthquake stress orientations. Many profiles exhibit the expected stress rotation signature (Fig. 1C) of a wide zone of high-pressure fluids (*29*), with far-field σ_H at 60° to 90° to the fault trend, and near-field σ_H at ~40°.

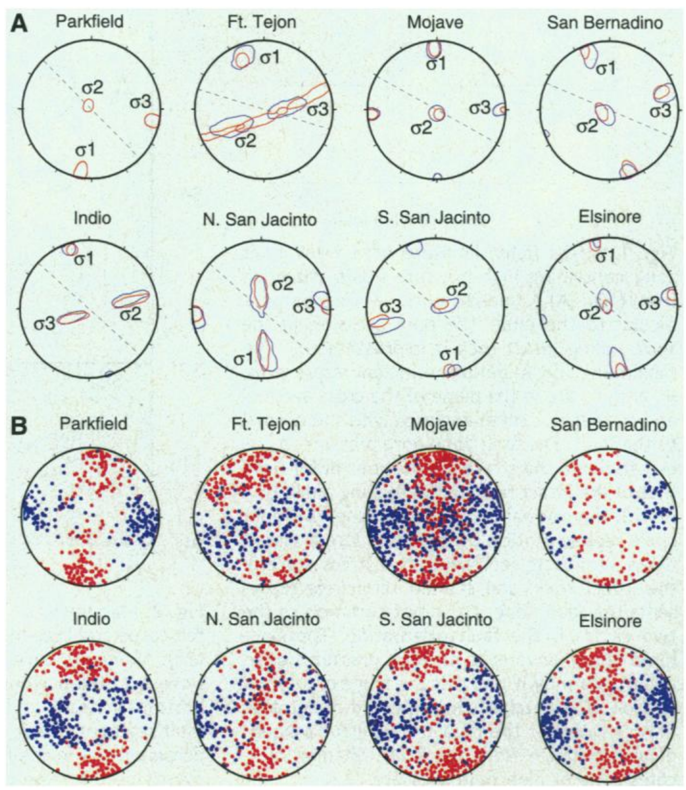

Fig. 4. Three-dimensional stress orientations along segments where σ_H is observed to be at low angle (≤60°) to the fault (Fig. 3). For the Parkfield segment, earthquakes in an 8-km-wide zone are inverted for stress; Fort Tejon, 23 km; Mojave, 10 km; San Bernadino, 4 km; Indio, 2 km; northern SJF, 4 km; southern SJF, 5 km; and EF, 3 km. (**A**) The 95% confidence regions for the maximum (σ_1), intermediate (σ_2), and minimum (σ_3) principal stress directions on a lower hemisphere projection. Red, all earthquakes inside the zone; blue, earthquakes with the best constrained mechanisms (M ≥ 2 events with ≥20 first-motion picks, about one-third of the data set). Dashed line indicates the strike of the fault segment. For all inversions, σ_1 is ≤60° to the fault. The close agreement of the two inversion results with each other and with the observations of Fig. 3 demonstrates the robustness of the observed stress orientations with respect to binning and data selection criteria. (**B**) Distribution of the compressional (red) and tensional (blue) axes of the focal mechanisms used in the inversion. The diverse set of mechanisms indicates that the observed stress orientations are not artifacts of inverting many similar fault-parallel, strike-slip mechanisms.

References and Notes

1. M. D. Zoback *et al.*, *Science* **238**, 1105 (1987); V. S. Mount and J. Suppe, *J. Geophys. Res.* **97**, 11995 (1992); G. J. Axen, *ibid.* p. 8979; M. E. Magee and M. D. Zoback, *Geology* **21**, 809 (1993); A. H. Lachenbruch and G. A. Thompson, *Earth Planet. Sci. Lett.* **15**, 116 (1972); J. N. Brune, T. L. Henyey, R. F. Roy, *J. Geophys. Res.* **74**, 3821 (1969); A. H. Lachenbruch and J. H. Sass, *ibid.* **97**, 4995 (1992).
2. M. K. Hubbert and W. W. Rubey, *Bull. Geol. Soc. Am.* **70**, 115 (1959).
3. J. D. Byerlee, *Pure Appl. Geophys.* **116**, 615 (1978).
4. D. E. Moore, D. A. Lockner, R. Summers, S. Ma, J. D. Byerlee, *Geology* **24**, 1041 (1996); C. Morrow, B. Radney, J. Byerlee, in *Fault Mechanics and Transport Properties of Rock*, B. Evans and T.-F. Wong, Eds. (Academic Press, San Diego, CA, 1992), pp. 69–88. Brucite is a current possibility [D. E. Moore, K. Iwata, H. Tanaka, D. A. Lockner, J. D. Byerlee, *Eos Trans. AGU* **78**, F732 (1997).]
5. T. H. Heaton, *Phys. Earth Planet. Inter.* **64**, 1 (1990).
6. Equivalent to typical earthquake stress drops of 3 to 10 MPa [H. Kanamori and D. L. Anderson, *Bull. Seismol. Soc. Am.* **65**, 1073 (1975)].
7. Estimated with the results of L. J. Sonder [*Tectonics* **9**, 769 (1990)] and modified slightly for shear stress anomalies.
8. M. D. Zoback *et al.*, *Nature* **365**, 633 (1993).
9. Assuming hydrostatic fluid pressure, lithostatic average stress and a coefficient of friction of 0.6, the deviatoric stress when the optimally oriented plane is at failure is one-third of lithostatic. Over seismogenic depths (0 to 12 km) the average lithostatic stress is ~150 MPa.
10. J. R. Rice, in *Fault Mechanics and Transport Properties of Rock*, B. Evans and T.-F. Wong, Eds. (Academic Press, San Diego, CA, 1992), pp. 475–503.
11. J. Byerlee, *Geophys. Res. Lett.* **17**, 2109 (1990).
12. The San Bernadino segment results disagree with left-lateral stress orientations measured to 3.5-km depth in the Cajon Pass borehole, ~5 km northeast of the SAF [M. D. Zoback and J. H. Healy, *J. Geophys. Res.* **97**, 5039 (1992); G. Shamir and M. D. Zoback, *ibid.* p. 5059]. However, shear-wave anisotropy observed at Cajon Pass [Y. Liu, S. Crampin, R. E. Abercrombie, *Geophys. J. Int.* **129**, 439 (1997)] implies that, although the shallow stress orientation is as observed in the borehole, σ_H at seismogenic depths is ~45° to the fault in a right-lateral sense.
13. M. Wyss and Z. Lu, *Geophys. Res. Lett.* **22**, 547 (1995); L. M. Jones, *J. Geophys. Res.* **93**, 8869 (1988).
14. H. Magistrale and C. Sanders, *J. Geophys. Res.* **101**, 3031 (1996); L. Seeber and J. G. Armbruster, *ibid.* **100**, 8285 (1995).
15. J. W. Gephart and D. W. Forsyth, *ibid.* **89**, 9305 (1984).
16. Using the far-field orientation of σ_H relative to the fault, the shear and normal stress on fault-parallel planes is found, assuming that the average stress is lithostatic, the pore pressure is hydrostatic, and the optimally oriented plane is at failure stress. The shear and normal stress on fault-parallel planes, assumed to be uniform, is used to find the pore pressure needed for the fault to fail under a Coulomb failure criterion with a coefficient of friction of 0.6.
17. F. M. Chester, J. P. Evans, R. L. Biegel, *J. Geophys. Res.* **98**, 771 (1993).
18. M. L. Blanpied, D. A. Lockner, J. D. Byerlee, *Nature* **358**, 574 (1992).
19. R. H. Sibson, *Tectonophysics* **211**, 283 (1992); J. Byerlee, *Geology* **21**, 303 (1993); N. H. Sleep and M. L. Blanpied, *Nature* **359**, 687 (1992).
20. C. A. Morrow and J. D. Byerlee, *J. Geophys. Res.* **97**, 5145 (1992).
21. M. Lisowski, J. C. Savage, W. H. Prescott, *ibid.* **96**, 8369 (1991).
22. K. E. Sieh, *Bull. Seismol. Soc. Am.* **68**, 1731 (1978).
23. W. Thatcher, in *The San Andreas Fault System, California: U.S. Geol. Surv. Prof. Paper 1515*, R. E. Wallace, Ed. (Government Printing Office, Washington, DC, 1990), pp. 189–205.
24. M. J. Unsworth, P. E. Malin, G. D. Egbert, J. R. Booker, *Geology* **25**, 359 (1997); T. Yukutake, *Earthquake Predict. Res.* **3**, 345 (1985); S. Handa and N. Sumitomo, *J. Geomag. Geoelectr.* **37**, 93 (1985); C. Thurber *et al.*, *Geophys. Res. Lett.* **24**, 1591 (1997); D. Zhao, H. Kanamori, H. Negishi, D. Wiens, *Science* **274**, 1891 (1996); D. Zhao and H. Negishi, *J. Geophys. Res.* **103**, 9967 (1998); G. S. Fuis *et al.*, *Eos Trans. AGU* **77**, 173 (1996); T. A. Stern and J. H. McBride, *Tectonophysics* **286**, 63 (1998).
25. R. F. Yerkes, P. Levine, C. M. Wentworth, *U.S. Geol. Surv. Prof. Paper 1487*, M. J. Rymer and W. L. Ellsworth, Eds. (Government Printing Office, Washington, DC, 1990), p. 235; F. A. F. Berry, *Am. Assoc. Pet. Geol. Bull.* **57**, 1219 (1973).
26. D. A. Lockner and J. D. Byerlee, *Pure Appl. Geophys.* **145**, 717 (1995).
27. E. Hauksson, unpublished data.
28. A. J. Michael, *J. Geophys. Res.* **92**, 357 (1987).
29. Other fluctuations in the observed stress orientations may be due to major earthquakes [D. A. Castillo and M. D. Zoback, *ibid.* **100**, 6249 (1995); E. Hauksson, *Bull. Seismol. Soc. Am.* **84**, 917 (1994)] or topography and density anomalies [L. J. Sonder, *Tectonics* **9**, 769 (1990)].

30. Supported by the Southern California Earthquake Center (SCEC), NSF Cooperative Agreement EAR-8920136, U.S. Geological Survey (USGS) Cooperative Agreements 14-08-0001-A0899 and 1434-HQ-97AG01718, and USGS grant 99HQGR0039. We thank H. Kanamori, L. M. Jones, J. Deng, M. D. Zoback, and S. Hickman for valuable reviews and A. J. Michael and J. W. Gephart for sharing their stress inversion programs. This is SCEC contribution 452 and Caltech DGPS contribution 8586.

18 November 1998; accepted 7 June 1999

Estimation of Particulate Organic Carbon in the Ocean from Satellite Remote Sensing

Dariusz Stramski,[1]* Rick A. Reynolds,[1] Mati Kahru,[2] B. Greg Mitchell[2]

Measurements from the Southern Ocean show that particulate organic carbon (POC) concentration is well correlated with the optical backscattering by particles suspended in seawater. This relation, in conjunction with retrieval of the backscattering coefficient from remote-sensing reflectance, provides an algorithm for estimating surface POC from satellite data of ocean color. Satellite imagery from SeaWiFS reveals the seasonal progression of POC, with a zonal band of elevated POC concentrations in December coinciding with the Antarctic Polar Front Zone. At that time, the POC pool within the top 100 meters of the entire Southern Ocean south of 40°S exceeded 0.8 gigatons.

The phenomenon of POC sinking from the surface ocean is part of the biological pump, which provides a mechanism for sequestration of carbon in the deep ocean (*1*), but it has been difficult to estimate the amount and distribution of POC at basin and global scales from ship-based surveys. Here, we show that POC can be estimated from satellites and use this approach to analyze POC dynamics in the Southern Ocean. Our approach is based on two relations: first, the dependence of the backscattering coefficient by particles suspended in seawater, $b_{bp}(\lambda)$, on the POC concentration, and second, the dependence of the spectral remote-sensing reflectance, $R_{rs}(\lambda)$, on the total backscattering coefficient of seawater, $b_b(\lambda)$ (*2*). Note that $b_b(\lambda) = b_{bw}(\lambda) + b_{bp}(\lambda)$, where $b_{bw}(\lambda)$ is a constant representing the backscattering coefficient of pure seawater and λ is light wavelength (expressed in nanometers).

To derive an algorithm, we collected data during two cruises of the U.S. Joint Global Ocean Flux Study (JGOFS) within the Antarctic Polar Front Zone (APFZ) along 170°W (between 50°S and 72°S) from January through March 1998, and one cruise within the Ross Sea in November and December 1997 along 76°30′S (169°E–178°W). The reflectance $R_{rs}(\lambda)$, defined as the ratio of upwelling radiance to downwelling irradiance just above the sea surface (*3*), was calculated from the underwater vertical profiles of downwelling irradiance and upwelling radiance measured with a MER-2040 spectroradiometer (*4*) (Biospherical Instruments, San Diego, California). The backscattering coefficient $b_b(\lambda)$ was obtained from measurements with a Hydroscat-6 sensor (*5*) (HOBI Labs, Watsonville, California), and the POC concentration was determined from the standard dry combustion analysis of samples that were taken with the ship's CTD (conductivity/temperature/depth)-rosette shortly before or after the optical casts. For the development of the satellite algorithm, only POC and $b_b(\lambda)$ measured within the top 15 m were used (typically from a depth of ~5 m).

POC and $b_{bp}(510)$ are highly correlated in both the APFZ and the Ross Sea, but the relation differs between the two regions (Fig. 1). The high correlation is caused by the dominance of the organic particle concentration in controlling changes in both POC and

[1]Marine Physical Laboratory and [2]Marine Research Division, Scripps Institution of Oceanography, University of California–San Diego, La Jolla, CA 92093–0238, USA.

*To whom correspondence should be addressed. E-mail: stramski@mpl.ucsd.edu